Plasma defect-engineering of bulk oxygen-deficient zirconia

Acta Materialia 262 (2024) 119457

Contents lists available at ScienceDirect

Acta Materialia

journal homepage: www.elsevier.com/locate/actamat

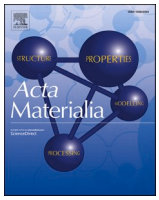

Full length article

Plasma defect-engineering of bulk oxygen-deficient zirconia

Behnam Dashtbozorg [a], Fangzhou Shi [a,*], Alberto Tagliaferro [b], Stephen Abela [c], Lucian Falticeanu [d], Hanshan Dong [a]

[a] School of Metallurgy & Materials, University of Birmingham, Birmingham B15 2TT, United Kingdom
[b] Department of Applied Science and Technology, Politecnico di Torino, Corso Duca degli Abruzzi 24, Turin 10129, Italy
[c] Department of Materials and Metallurgy Engineering, Faculty of Engineering, University of Malta, Msida, MSD 2080, Malta
[d] Precision Ceramics UK Limited, Birmingham B19 3PA, United Kingdom

ARTICLE INFO

Keywords:
Yttria-stabilized zirconia polycrystal
Low-pressure plasma
Electron paramagnetic resonance
X-ray photoelectron spectroscopy (XPS)
Optical spectroscopy

ABSTRACT

Oxygen-deficient zirconia (ZrO_{2-x}) has recently emerged as a promising material for light absorption and photocatalytic applications. However, the economic and environmentally friendly manufacture of bulk ZrO_{2-x} remains challenging and has limited widespread adoption. In this study, we present a novel low-pressure (300 Pa) plasma treatment (H_2 gas at 500 °C for 5 h) capable of producing fully-dense bulk ZrO_{2-x} without significant structural modifications. EPR (electron paramagnetic resonance) and XPS (X-ray photoelectron spectroscopy) characterisation of the plasma treated zirconia indicate the formation of Zr^{3+} ions and F^{2+} ($V_{\ddot{O}}$) centres. The increase of oxygen vacancies is also supported by the greater exothermic heat flow and relative mass gain observed through TGA (thermogravimetric analysis) and DSC (differential scanning calorimetry) analyses. Diffuse reflectance spectroscopy (DRS) reveals a substantial enhancement in light absorption, with an average increase of 66.2 % and >65 % absolute absorption across the entire spectrum (200–3000 nm). XPS and DRS measurements suggest significant reduction in both direct (from 4.84 to 2.61 eV) and indirect (from 3.19 to 1.45 eV) bandgap transition. By effectively enhancing the light absorption capability, reducing bandgap transitions, and maintaining the structural integrity of zirconia, low-pressure plasma treatments offer a promising and scalable approach for the environmentally friendly production of next-generation ZrO_{2-x} materials.

1. Introduction

Semiconductor-based technologies hold great promise for meeting the increasing demands for renewable and green energy. Significant research efforts have been directed towards developing future solutions, at both material and device level, capable of harvesting or producing energy from sustainable sources [1–3]. Numerous studies have already demonstrated the potential for semiconducting materials to act as solar energy harvesters or photocatalytic materials, for instance for the efficient generation of hydrogen from water [4,5]. However, when compared to commonly studied materials such as silicon and titanium dioxide, pristine zirconia is not typically considered an attractive solution for energy applications. The relatively wide bandgap of zirconia (approximately 5-6 eV) does not readily facilitate the initiation or catalysis of typical reactions involved in these applications [6–11]. Fortunately, recent breakthroughs using defect-engineering techniques have demonstrated the possibility to reduce the bandgap of zirconia by introducing large densities of oxygen vacancies (e.g., down to 2.52 eV in a study by Sinhamahapatra, et al. [12]). Such modifications can create new donor energy levels between the valence and conduction bands (known as mid-gap states), and consequently, transforms the electrically insulating zirconia into an n-type semiconducting material [13]. The narrow bandgap of oxygen-deficient zirconia (ZrO_{2-x}) enables the absorption of photons with longer wavelengths, which also increases the photoresponsive range of the material. This has generated substantial interest for the use of ZrO_{2-x} as a future photocatalytic material for the splitting of water to generate clean hydrogen, for the decomposition of CO_2 to reduce greenhouse gases, and for the formation of reactive oxygen species (e.g., superoxide ions, hydroxyl radicals and peroxides) [14–18].

Although oxygen-deficient zirconia has many encouraging properties, the challenges to efficiently produce oxygen vacancies in zirconia have limited its widespread adoption. This barrier corresponds to the high energy requirements for the dissociation of Zr-O bonds, with

* Corresponding author.
E-mail address: fxs701@student.bham.ac.uk (F. Shi).

https://doi.org/10.1016/j.actamat.2023.119457
Received 21 August 2023; Received in revised form 13 October 2023; Accepted 20 October 2023
Available online 21 October 2023

reported bond dissociation energies of 7.7–7.9 eV [19,20] and bulk vacancy formation energies of 8.5–9.1 eV [12,21–24]. Consequently, oxygen deficient zirconia has largely been confined to research environments, where significant efforts have been dedicated to developing new highly efficient and cost-effective manufacturing routes. Two promising approaches are the Zu, et al. [13] and Wang, et al. [25] methods, both of which make use of zirconia particle/powder precursors. In the Zu, et al. [13] method, oxygen-deficient zirconia nanoparticles are produced through molten lithium reduction of pure zirconia disks at 400 °C under high-purity argon gas. Once the zirconia turns black, impurities are removed by repeated washing with HCl, ethanol, and deionised water, followed by ultrasonication to return them to nanoparticles. The Wang, et al. [25] approach produces black oxygen-deficient zirconia through high-pressure torsion straining (6 GPa for 2 turns at 400 °C) of yttria-stabilised zirconia powders, which forms a thin, dense, and highly distorted layer of material (due to plastic deformation, lattice defects and phase transformation events).

In addition to the above mentioned approaches, various other techniques have also been explored for introducing oxygen vacancies into zirconia, including electric (or flash) sintering [9,26,27], high-temperature carbon reduction [28], cationic doping [29–31], Ar^{+} bombardment [32], magnesiothermic reduction [12,15], and electrochemical reduction [33–39]. Each of these methods offer alternative pathways to reduce the bandgap of zirconia and improve its photoresponsivity. It is important to note that, other than the electrochemical reduction methods, the other listed approaches have only been demonstrated to work with zirconia in the form of powders, nanotubes, or disks. This can create significant barriers for use of dense oxygen-deficient zirconia in future industrial applications. Moreover, many of the listed approaches involve demanding processing conditions such as high pressures and temperatures or the use of strong reducing agents (e.g., acids), thereby creating environmental concerns about their safe usage and proper disposal if such methods were to be upscaled [12, 40].

Electrochemical reduction techniques, which can form oxygen vacancies in solid zirconia, have shown promising results for rapidly forming dense sheets of oxygen-deficient zirconia. By applying a voltage difference at two ends of the material, it is possible to generate oxygen vacancies at the anode-facing end and propagate them towards the cathode-facing end [9,27,33,36,41]. As the electrodes must be in direct contact with the ends of the material, this can generate a tri-layer junction across the specimen when applying large potential differences, leading to the potential development of n-type conductivity at the cathode-end, p-type conductivity at the anode-end, and a largely unchanged bulk [42,43]. High-temperature electrochemical reduction methods utilising voltage biases and manipulating boundary conditions have been shown to be able to effectively bypass this tri-layer configuration [44]. The major advantage of the electrochemical reduction approach is the ability to utilise commercially available solid zirconia sheets for the transformation into identically shaped and sized oxygen-deficient zirconia sheets. In this way, it is more convenient and cost-effective to showcase the potential of oxygen-deficient zirconia, as well as to significantly reduce the barriers for future upscaling and industrial adoption. In addition, the direct production of solid products bypasses the challenges related to the efficient sintering of oxygen-deficient zirconia powders without re-oxidation. However, existing electrochemical reduction routes pose challenges for the homogeneous treatment of components with complex geometries (non-uniform potential difference) or for the low-temperature formation of fully n-type or p-type semiconducting oxygen-deficient zirconia (due to the directional growth and the potential tri-layer structure).

Low-pressure direct current (DC) plasma treatments, which are traditionally used to modify the surfaces of metallic materials [45–47], also involve the use of a potential difference across an anode and a cathode. In the case of low-pressure DC plasma treatments, this potential difference leads to the formation of a conductive gas medium (plasma), which completes the circuit, and enables the acceleration of positive ions (towards the cathode) and electrons (towards the anode). As the gas-medium can carry the charge across the cathode and anode, there are no requirements for the physical connection of the electrodes [48]. Therefore, low-pressure DC plasma treatments can be considered a unique form of electrochemical treatment that has the potential to bulk-reduce zirconia materials under certain conditions (such as pressure, gas mixture, and power) [41,49]. However, as electrically conductive materials are traditionally required for DC plasma treatments, no studies have explored the feasibility of DC plasma treatments to transform pristine zirconia into oxygen-deficient zirconia [48].

Thus, the aim of this study is to investigate the potential of low-pressure DC plasma treatments to reduce solid polycrystalline zirconia into oxygen-deficient zirconia. As the feasibility of the plasma treatment and the comprehensive characterisation of the treated material are the focus of this study, a simple plasma treatment protocol has been chosen (100 % hydrogen plasma treatment under a fixed temperature of 500 °C and gas pressure of 300 Pa).

2. Methods

2.1. Sample preparation

Yttria-stabilised (3 mol%) zirconia rods (10 mm diameter; Precision Ceramics UK) were abrasion cut (Struers Accutom 50) using cubic boron nitride cutting wheels to produce 3 mm thick cylindrical samples. Samples were subsequently flattened and ground (up to #4000 grit size) using SiC abrasive paper. Prior to plasma treatment, samples were polished using diamond suspensions (down to 1 μm). Ultrasonic cleaning using liquid detergent and acetone were carried out to remove contaminants between each stage.

2.2. Low-pressure DC plasma treatment

Plasma treatments were conducted using a Klöckner Ionon 20 kVA DC plasma furnace at a treatment temperature of 500 °C using the following parameters of 550 V, ≈1 A, 100 % H_2 gas atmosphere, and working gas pressure of 3 mbar (300 Pa). Zirconia samples were positioned directly onto the stainless-steel worktable (cathode) and treated for 5 h (Fig. 1). After the plasma treatment, samples were gently polished using 1 μm diamond suspensions to remove loose deposited material (due to sputtering from the worktable).

2.3. X-ray diffraction (XRD)

Crystallographic phase analysis was performed using a Proto AXRD benchtop X-ray diffractometer fitted with a Cu radiation source (Kα = 0.15406 nm). Measurements were performed between the 2θ values of 20 ° and 80 ° using step increments of 0.01493 ° XRD data was analysed using the PANalytical Highscore Plus software (with the ICDD PDF-2 database).

2.4. Raman spectroscopy

Identification of the near surface chemistry, phase structure (tetragonal to monoclinic transformation) and light absorption capabilities of the zirconia materials was performed using a Renishaw inVia Raman microscope fitted with a 532 nm excitation laser source and groove density of 1800 l/mm. Raman spectra were collected in the Raman shift range 100–800 cm^{-1}. Decomposition of the Raman spectra was performed using the Renishaw WiRE software package to determine peak centre positions and FWHM (full width at half maximum) of each component before and after plasma treatment of the zirconia. Light absorption capability calculations were obtained by comparing the area of each deconvoluted component of the spectra obtained from untreated and plasma treated zirconia (using the CasaXPS software package). The

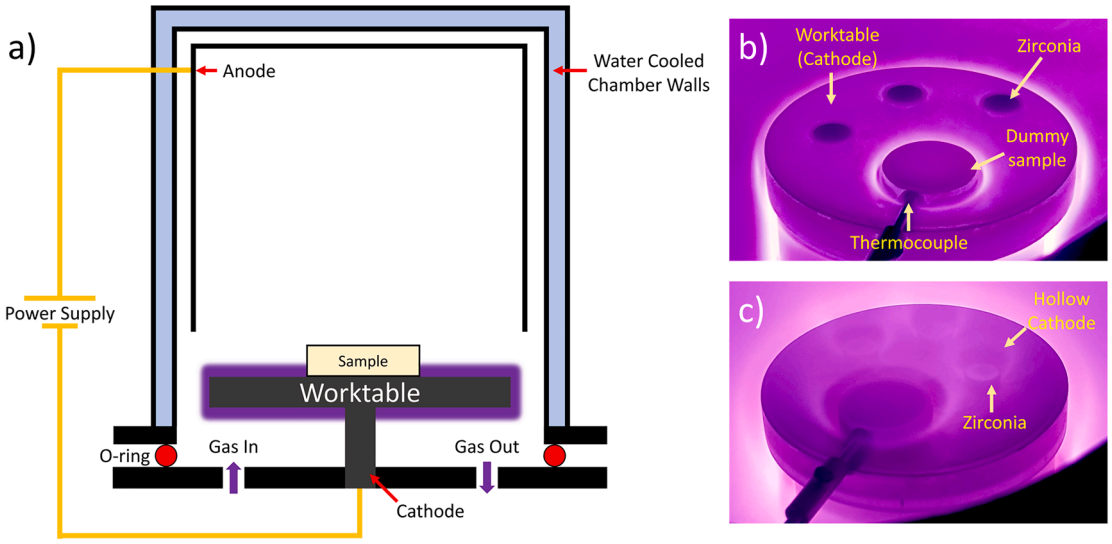

Fig. 1. Schematic diagram of the DC plasma treatment configuration (a). Initially, the glow-discharge plasma only forms on the cathodic worktable (b). However, as the treatment progresses, (c) the glow-discharge also begins to form on the zirconia specimen (as indicated by the hollow cathode formation).

relative change in area under the curve for each fitted component following plasma treatment was compared with untreated zirconia to calculate the average percentage change in total emitted light.

2.5. Electron paramagnetic resonance (EPR) spectroscopy

Paramagnetic centres in the zirconia were investigated using EPR spectroscopy (ELEXSYS-II EPR spectrometer) at room temperature using a N_2 atmosphere at a X-band frequency of 9.84 GHz, modulation amplitude of 1 G (0.1 mT) and microwave power of 3.99 mW. Patterns were generated around a 3500 G central magnetic field, with a sweep width of 150 G and sweep time of 30 s.

2.6. X-ray photoelectron spectroscopy (XPS)

Changes in the bonding environment of Zr and O atoms within the zirconia samples following plasma treatment were investigated using XPS spectroscopy (Thermo Scientific Nexsa XPS) fitted with a monochromatic Al X-ray Kα (1486.6 eV) X-ray source. Valence band (VB) energy levels of the zirconia samples were revealed by low energy XPS spectroscopy (up to 10 eV with an energy step size of 0.1 eV). High resolution scans (energy step size of 0.05 eV) were used to characterise the bonding environment of Zr 3d (178–188 eV) and O 1 s (526–538 eV) electrons. C1s (284.6 eV) scan correction was performed for all spectra to account for charging of the samples. Deconvolution and analysis of XPS spectra was performed using the CasaXPS software package. Monte Carlo error analysis was used to test the validity of the modelled components and to calculate the standard deviation of the area compositions. Further information regarding the fitting parameters and error analysis can be found in §S2.1 of the supplementary information.

2.7. Thermal analysis

Simultaneous thermal analysis (STA) measurements were carried out to determine the mass and heat flow changes of the samples upon heating. Both thermogravimetric analysis (TGA) and differential scanning calorimetry (DSC) data were measured on untreated and plasma treated zirconia (recorded simultaneously) using a Netzsch STA 449F3. STA measurements were performed in air using plate samples of dimensions of 2 mm in length, 2 mm in width and 0.5 mm in thickness (placed in a platinum crucible). Samples were heated to 500 °C at a heating rate of 10 °C/min, and then held at 500 °C for 10 h, before passively cooling down to room temperature. An empty run was performed to account for the background noise contributions of the measurements (e.g., due to weight and heat flow errors within the system). To reduce the initial influence of contaminants (e.g., adsorbed moisture) during the heating up process, relative mass change was normalised to the measured mass at 100 °C for the heating up stage and to the measured mass at the beginning of the holding stage (at 500 °C).

2.8. Optical absorption measurement

The photon absorption behaviour of untreated and plasma treated zirconia were measured by diffuse reflectance spectroscopy (DRS) across the UV–Vis-NIR-SWIR (ultraviolet – visible – near-infrared – shortwave infrared) range with a Shimadzu SolidSpec-3700 spectrophotometer fitted with an integrating sphere. DRS was utilised to bypass the opaque nature of the material, with spectra being obtained between wavelengths of 200–3000 nm, using a step size of 1 nm and medium scan speed. As suggested by several recent studies [50–52], a combination of the Tauc method and Kubelka-Munk function were used to determine the allowed direct and indirect transitions (further information regarding the method and justifications are provided in §S3 of the supplementary information).

3. Results and discussion

Dense sintered oxygen-deficient zirconia with a small bandgap has tremendous potential to create new opportunities for the development and expansion of zirconia as an energy harvesting and oxygen sensing (particularly at lower temperatures) material of industrial interest. To explore the potential for low-pressure DC plasma treatments to bulk reduce dense 3 mol% yttria-stabilised zirconia, the findings of this study structured to discuss (1) the visual, crystallographic, and structural characteristics of the plasma treated zirconia, (2) to confirm the formation of oxygen vacancies and the reduction of the zirconium ions, and (3) to characterise the electronic band structure and light absorption capability of the plasma treated zirconia.

3.1. Visual, crystallographic, and structural changes

The complete colour transformation of the zirconia, going from a pure white to a metallic black, is the most striking visual modification following plasma treatment (Fig. 2). The through-depth nature of the

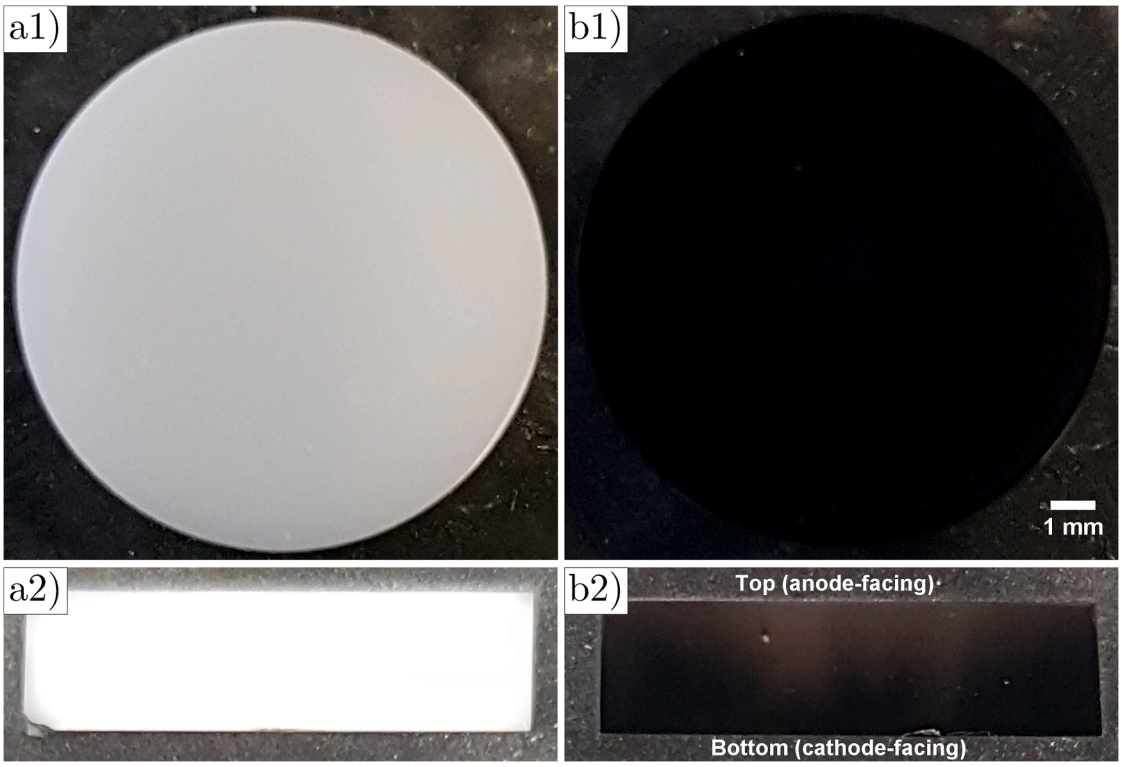

Fig. 2. Camera images of (a) untreated and (b) plasma treated zirconia from the bottom surface (labelled 1) and cross-sectional (labelled 2) views are shown. The bottom surface images (a1 and b1) clearly illustrate the complete transformation of zirconia from white to black after plasma treatment. The cross-sectional views reveal an internal colour gradient, with the bottom surface facing the cathode appearing darker and the top surface facing the anode appearing lighter.

blackening process (i.e., entire transformation of the sample) was revealed by cross-sectional observations (Fig. 2b2). The gradient of blackening, with darker colours near the bottom surface (cathode-facing), suggests a similar directional growth route as other electrochemical reduction approaches (growth from the cathode towards the anode) [33]. The colour variations between the centres and edges of the sample also suggest a preferential transformation mechanism during the treatment, potentially arising due to electrical potential variations across the cathode-facing surface. Although the distinct colour transformation of zirconia implies that oxygen-deficient zirconia has formed, more direct confirmation of the transformation was revealed via EPR, XPS and DSC/TGA analysis can be found in §3.2 [53].

Despite the remarkable morphological change in colour, no formation of new phases could be identified under XRD analysis (Fig. 3a). The varying densities of oxygen vacancies across the untreated and plasma treated zirconia samples gave rise to different localised stoichiometries (i.e., ZrO_{2-x}, where x varies but remains <2), which could not be wholly indexed by any single XRD reference pattern. However, no unidentifiable (or satellite) peaks belonging to structures other than tetragonal phase zirconia or yttria-stabilised zirconia were found. Moreover, no

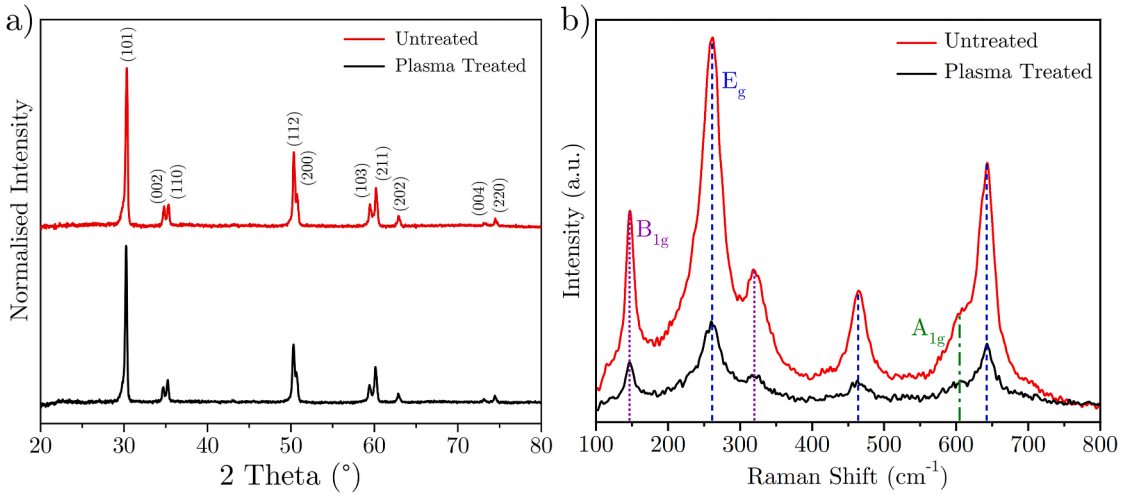

Fig. 3. The (a) XRD and (b) Raman spectra of untreated and plasma treated zirconia are shown. The typical locations of the B_{1g} (dotted), E_g (dashed), and A_{1g} (dotted and dashed) vibrational modes of zirconia are indicated within the Raman spectra. No change in structure or peak shift can be observed under either XRD or Raman spectroscopy. However, the measured light intensity under Raman spectroscopy is significantly reduced following plasma treatment, resulting in a poor signal-to-noise ratio under the same settings.

significant large shift in d-spacing or broadening of peaks were observed, with no change or only minor change of the long range order developed following the plasma treatment of zirconia [13,25,54].

The Raman spectra of the untreated and plasma treated zirconia (Fig. 3b) indicated no detectable change in the chemical structure, formation of new peaks, or significant displacement of existing peak centres. Both untreated and plasma treated zirconia only exhibited characteristic peaks assigned to the different vibrational modes of 3 mol % yttria-stabilised zirconia (Fig. 3b), including three E_g modes (260.2, 464.8, 642.7 cm^{-1}), two B_{1g} modes (147.0, 323.0 cm^{-1}) and one A_{1g} mode (609.2 cm^{-1}), which all belong to the $P4_2/nmc$ space group [31,55]. Deconvolution and fitting of the spectra suggests no consistent or obvious displacement or broadening of the peaks (outlined in §S1 of the supporting information) and suggests that there is no significant long-range distortion of the lattice, which aligns with the XRD measurements [56]. The most noticeable difference between the two zirconia samples is the significant reduction in reflected light intensity observed in the plasma treated sample, which will be discussed in §3.3.

3.2. Confirming the oxygen-deficiency of plasma treated zirconia

3.2.1. EPR detection of F centres & reduced zirconium

Oxygen vacancies are common phenomena in many oxides, with their formation giving rise to properties such as increased ionic conductivity and light absorption capability. Despite their classification as a crystallographic point defect of the material, the controlled existence of vacancies can give rise to beneficial physical and mechanical properties, zirconia doped with yttria (Y_2O_3) being an excellent example [23]. The difference in oxidation states of zirconium (Zr^{4+}) and the yttrium (Y^{3+}) ions means that, for every two yttrium ions that displace zirconium ions ($2Y'_{Zr}$), an oxygen vacancy ($V_O^{\cdot\cdot}$) must be formed in the lattice to preserve charge neutrality (Eq. (1)) [57]. The combination of the larger ionic radii of yttrium and the reduction of interlaminar stresses (due to the vacant oxygen sites) gives rise to the "pinning" of the tetragonal or cubic phase at room temperature [58]. The stability (or metastability) of these high temperature phases give rise to many of the advantageous properties (e.g., high fracture toughness) that differentiate zirconia to other ceramics.

$$Y_2O_3 \xrightarrow{ZrO_2} 2Y'_{Zr} + V_O^{\cdot\cdot} + 3O_O^X \quad (1)$$

Due to the profound influence that these oxygen vacancies have on the overall colour of the material, such defects are typically called F centres or colour centres [39]. F centres are primarily identified according to their relative charge (as compared with the occupation of the site with an O^{2-} ion), and therefore three main configurations exist: the F^{2+} ($V_O^{\cdot\cdot}$; 0 trapped electrons), F^+ ($V_O^{\cdot}$; 1 trapped electrons), and F centres (V_O^X; 2 trapped electrons) [38]. Further subcategorisation of the F centres can also be performed depending on the location (e.g., surface or bulk), vicinity to other vacant sites (e.g., neighbouring oxygen vacancies), and the displacement of neighbouring cationic sites [59].

Electron paramagnetic resonance (EPR) spectroscopy presents as the most commonly used method to identify F centres; however, as EPR signals depend on the presence of unpaired electrons, only paramagnetic F^+ centres with single trapped electrons can be measured, while F and F^{2+} centres remain invisible to EPR [11,37,60,61].

Depending on the oxidation state of neighbouring cations, EPR spectra can also help to detect the presence of cations with unpaired electrons. In the case of zirconia, this can allow the presence of Zr^{3+} ions to be detected. Although there are many more pathways for forming Zr^{3+} ions (dehydration of OH^- groups), we showcase 2 possible routes for their formation in the presence of F^+ (Eq. (2)) and F^{2+} (Eq. (3)) centres [9,28,53].

$$ZrO_2 \rightarrow Zr^{3+} + O_O^X + V_O^{\cdot} + \frac{1}{2}O_2 \quad (2)$$

$$2ZrO_2 \rightarrow 2Zr^{3+} + 3O_O^X + V_O^{\cdot\cdot} + \frac{1}{2}O_2 \quad (3)$$

Fig. 4 displays the EPR spectra, and reveals significant formation of new paramagnetic centres after plasma treatment of the zirconia. The decomposition of the spectra indicates the presence of two underlying signals at g-tensor values of $g_\perp = 1.9785$ (signal 2) and $g_\parallel = 1.9763$ (signal 3). These values closely align with previous reports of Zr^{3+} ions (d^1 ion) within bulk tetragonal phase zirconia [11,25,37,54,62–66]. Moreover, both untreated and plasma treated zirconia exhibit an isotropic peak (signal 1) at g-tensor values of 2.0040 (g_1(U)) and 2.0039 (g_1(PT)), respectively. EPR studies on zirconia in powder form typically associate signals close to this g-factor with surface adsorbed superoxide ions (O_2^-), which can result from the oxidation of Zr^{3+} back to Zr^{4+} (Eq. (4)). If this signal corresponded to superoxides, an increase of the signal would be expected following the reduction of the zirconium ions after plasma treatment. Therefore, as this trend is not observed, this suggests that the signal does not correspond to the adsorption of superoxides. Furthermore, superoxides usually exhibit a set of three peaks at g-factors approximately equal to 2.0336 (g_{zz}), 2.0096 (g_{yy}), and 2.0034 (g_{zz}), which are also not found in the zirconia samples of this study [11,64].

$$Zr^{3+}_{(surf)} + O_{2(gas)} \rightarrow Zr^{4+}_{(surf)} + O^-_{2(ads)} \quad (4)$$

F^+ centres have also been suggested to exhibit peaks between g-tensor values of 2.002 and 2.004 and can be expected to form following the plasma treatment of zirconia (Eq. (2)) [30,64,67,68]. The lack of an increase in signal 1 can be explained by the preferential formation of diamagnetic F^{2+} centres under plasma treatment (Eq. (3)) [69]. These F^{2+} centres would give rise to EPR-elusive vacancies that would not contribute to the intensity of the measured spectra. However, given the significant increase in Zr^{3+}, this suggests that F^{2+} centres must form in the bulk of plasma treated zirconia, while F^+ centres are confined to defect sites on the surface or in the bulk (e.g., grain boundaries) of the material [67].

As signal 1 is present (and at a similar intensity) in untreated zirconia, the conversion of any pre-existing F^+ centres to F^{2+} centres would

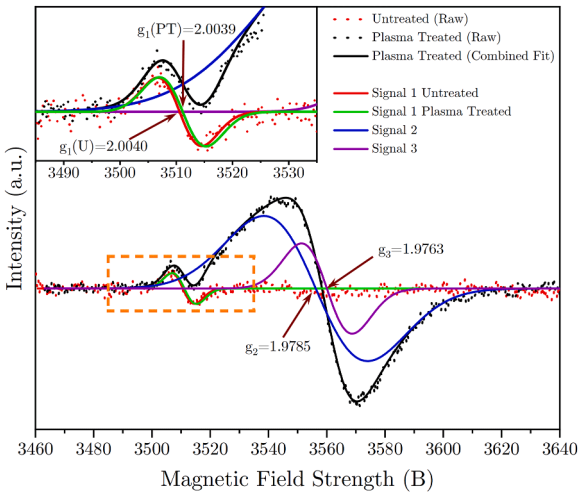

Fig. 4. EPR spectra of untreated and plasma treated zirconia are displayed, showing the raw data as dots and the fitted data as lines. In both untreated and plasma treated zirconia, a peak (signal 1) is observed near the g-tensor of a free electron (g_e) with fitted g-factors of 2.0040 (g_1(U)) and 2.0039 (g_2(PT)), respectively. The inset in the top left provides a magnified view of the dashed region corresponding to this signal. Following plasma treatment, new paramagnetic centres (signals 2 and 3) associated with the formation of Zr^{3+} are detected at g-tensors of 1.9785 (g_2) and 1.9763 (g_3). The similar intensity of signal 1 for both untreated and plasma treated zirconia suggests that the reduction process preferentially leads to the formation of diamagnetic F^{2+} centres, as indicated by Eq. (3).

be expected to result in a reduction of signal 1. However, no noticeable change in signal 1 is observed following plasma treatment of the zirconia. This suggests that either the site of the paramagnetic centres corresponding to signal 1 are not affected by the plasma treatment or they are re-established when the samples are exposed to atmospheric conditions [70]. This supports the idea that these paramagnetic centres correspond to surface defects (especially as both tested sample types have similar surface areas). However, a more in-depth evaluation of these paramagnetic sites is necessary to identify the origin of these signals (e.g., by way of scanning tunnelling microscopy or environmentally controlled EPR measurements).

3.3. XPS evaluation of oxygen and zirconium bonding environment

In agreement with the EPR analysis, the XPS (X-ray photoelectron spectroscopy) measurements also suggest the reduction of zirconium ions ($Zr^{4+} \rightarrow Zr^{3+}$) and the increased formation of oxygen vacancies.

Deconvolution of the O 1 s spectra in Fig. 5 reveals the presence of three distinct peaks, labelled as O1, O2, and O3, for both untreated and plasma treated zirconia [13]. Consistent with the literature, which is reviewed in §S2.2 of the supporting information, these peaks have been assigned to specific components. Specifically, O1 corresponds to lattice oxygen in zirconia, O2 corresponds to surface adsorbed hydroxyl groups, and O3 corresponds to surface adsorbed molecular water.

Non-dissociative adsorption of water occurs through hydrogen bonding with occupied zirconia lattice sites and is not typically associated with the reduction (or oxidation) of the adsorption site. On the other hand, in the presence of oxygen vacancies, molecular water can undergo dissociation, resulting in the formation of a hydroxyl group that occupies the vacant site and a hydrogen atom that bonds with a nearby lattice oxygen, thereby forming another hydroxyl group. This dissociative adsorption of water onto zirconia surfaces containing oxygen vacancies (V_O and V_O^X) can lead to the reduction of zirconium ions, as shown in Eqs. (5) and (6), respectively [70].

Under ambient conditions, dissociative adsorption of water is energetically more favourable than non-dissociative adsorption. Therefore, surfaces with higher densities of oxygen vacancies are expected to exhibit lower amounts of adsorbed molecular water (O3) but higher concentrations of surface adsorbed hydroxyl groups (O2) and Zr^{3+}. Therefore, when analysing oxygen vacancies using XPS, it is important to consider changes in both the oxygen and zirconium bonding environments [71].

$$Zr_{Zr}^{X} + V_O^{\cdot} + O_O^{X} + H_2O \rightarrow 2(OH)_O^{\cdot} + Zr_{Zr}^{'} \quad (5)$$

$$2Zr_{Zr}^{X} + V_O^{X} + O_O^{X} + H_2O \rightarrow 2(OH)_O^{\cdot} + 2Zr_{Zr}^{'} \quad (6)$$

The analysis of the fitted components of the O 1 s spectra for both untreated and plasma treated zirconia samples shows no significant positional shift, with binding energy displacements of 0.1 eV for O1, 0.1 eV for O2, and 0.2 eV for O3. This observation is consistent with other published findings on modified zirconia [72,73]. Additionally, the error analysis of the fitted components also indicates the good validity of the models, with a maximum area composition standard deviation of 0.26 %.

Fig. 5 and Table 1 illustrate the most significant difference between the O 1 s spectra of untreated and plasma treated zirconia, which lies in the concentrations of the different components (O1, O2, and O3). While the O1 component remains relatively unchanged, with a slight increase from 18.7 ± 0.3 % to 19.5 ± 0.2 % following plasma treatment, notable modifications arise in the O2 and O3 components. The O2 component shows a significant increase from 25.5 ± 0.2 % to 37.8 ± 0.2 %, which represents a 12.3 % increase, whereas the O3 component decreases from 55.8 ± 0.3 % to 42.7 ± 0.3 %, indicating a 13.1 % decrease. Therefore, this combined change in composition, along with the corresponding changes observed in the Zr 3d spectra (discussed in the following paragraphs), demonstrates an overall increase in surface hydroxyl groups (O2) and a decrease in surface adsorbed water (O3) following plasma treatment.

The Zr 3d spectra (Fig. 6) exhibits two sets of doublet peaks ($3d_{3/2}$ and $3d_{5/2}$) corresponding to Zr^{4+} and Zr^{3+} in both untreated and plasma treated zirconia [13,38,41,54]. Consistent with previous studies, the Zr $3d_{3/2}$ peak is observed at an energy approximately 2.4 eV higher than the Zr $3d_{5/2}$ peak for both oxidation states and sample types. Error analysis using Monte Carlo simulations demonstrates a high quality of fit, with a maximum deviation in area composition of 0.09 % across all the modelled components for both spectra. The Zr^{4+} $3d_{5/2}$ peak remains

Table 1
Normalised compositions of the different fitted components of the O 1 s and Zr 3d spectra of untreated and plasma treated zirconia.

Spectra and Component		Composition (%)	
		Untreated	Plasma Treated
O 1s	**O1**	18.7 ± 0.3	19.5 ± 0.2
	O2	25.5 ± 0.2	37.8 ± 0.2
	O3	55.8 ± 0.3	42.7 ± 0.3
Zr 3d	**Zr^{4+}**	59.6 ± 0.1	30.7 ± 0.1
	Zr^{3+}	40.4 ± 0.1	69.3 ± 0.1

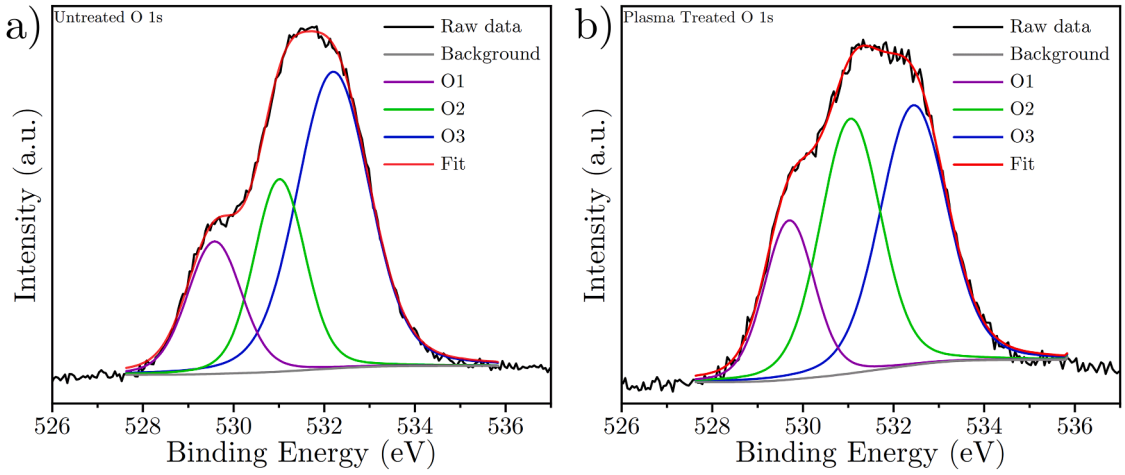

Fig. 5. Oxygen O 1 s spectra of (a) untreated and (b) plasma treated zirconia. After plasma treatment, there is a notable increase in the intensity of adsorbed surface hydroxyl groups (O2) and reduction of molecular water (O3), which suggests that more oxygen vacancies are present on the surface of the plasma treated zirconia.

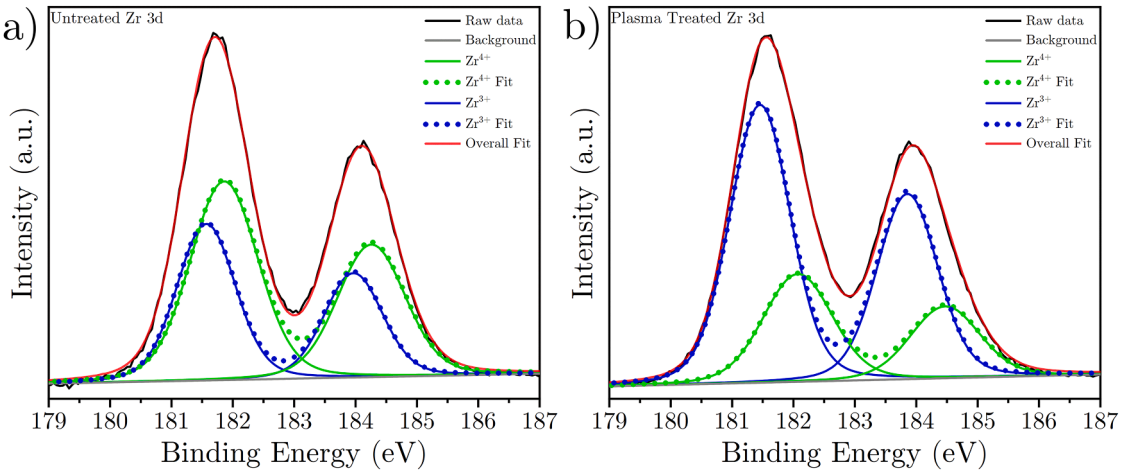

Fig. 6. Zirconium Zr 3d spectra of (a) untreated and (b) plasma treated zirconia are exhibited, and reveal a significant shift in surface composition of Zr^{4+} and Zr^{3+}, with the reduced state dominating after plasma treatment. Consistent with the observations in Fig. 5, the increased concentration of the Zr^{3+} components corroborate with the increase of oxygen vacancies.

relatively unchanged, with binding energies measured at 181.9 eV and 182.1 eV for untreated and plasma treated zirconia, respectively. Similarly, the Zr^{3+} $3d_{5/2}$ peak shows no significant shift, with fitted binding energies at 181.6 eV and 181.5 eV for untreated and plasma treated samples, respectively. As indicated under Table 1, the proportion of Zr^{3+} significantly increases following plasma treatment of the zirconia, shifting from 40.4 ± 0.1 % (i.e., more Zr^{4+} than Zr^{3+}) to 69.3 ± 0.1 % (more Zr^{3+} than Zr^{4+}) at the surface. In combination with the observations from the O 1 s spectra, these results indicate that the concentrations of Zr^{3+} and O2 increase, while the concentration of O3 decreases, which all suggest a substantial increase in oxygen vacancies on the surface of zirconia after plasma treatment.

3.4. *Thermal analysis of oxygen-deficiency*

The oxygen-deficient nature of the plasma treated zirconia was investigated using simultaneous TGA and DSC analysis in two consecutive stages: (1) heating from 100 to 500 °C and (2) isothermal holding at 500 °C for 10 h. The thermal gravimetric (TG) curves during the heating process (Fig. 7a) exhibit distinct differences between untreated and plasma treated zirconia. The untreated zirconia shows a simple trend with a linear increase in relative mass up to 425 °C, followed by a sharp reduction. In contrast, the plasma treated zirconia demonstrates a more complex curve composed of a linear increase up to 240 °C, a slight plateau up to 300 °C, a further increase up to approximately 400 °C, before a final flattening of the curve close to 500 °C.

The corresponding heat flow curves (Fig. 7a) closely reflect the relative mass changes of both samples. For the untreated zirconia, the heat flow remains predominantly flat (or slightly negative) up to 410 °C, corresponding to the linear mass gain region of the TG curve, followed by a gradual exothermic increase up to 500 °C (aligned with the reduction of relative mass). The mass loss and exothermic heat flow between 410 and 500 °C in the untreated sample can be attributed to the reduction (oxygen removal) of zirconia at elevated temperatures [74, 75].

On the other hand, the heat flow trend of the plasma treated zirconia remains (mostly) flat up to 275 °C, followed by an endothermic reaction between 275 and 400 °C and a subsequent plateau up to 500 °C. The presence of the endothermic reaction and reduction in relative mass between 275 and 400 °C is consistent with published phase diagrams of 3 mol% yttria-stabilised zirconia, indicating a monoclinic-to-tetragonal phase transformation within this temperature range [58,74–76]. It is worth noting that no monoclinic phase was identified in the XRD or Raman analysis (Fig. 3), and the limited deflection of the heat flow curve

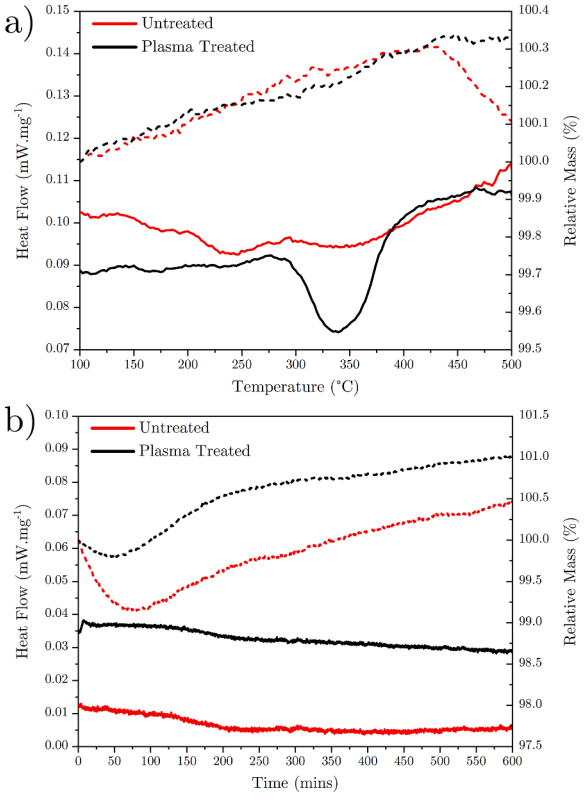

Fig. 7. Heat flow (line) and thermogravimetric (dotted) curves for (a) non-isothermal heating to 500 °C and (b) isothermal holding at 500 °C of untreated and plasma treated zirconia. The plasma treated zirconia exhibits a more pronounced and sustained increase in mass under both testing methods. Additionally, an endothermic reaction (275–400 °C) is observed for the plasma treated zirconia during the heating up stage, which corresponds to a monoclinic-to-tetragonal phase transformation. The relative mass is normalised with respect to the measured mass at the start of each respective stage.

suggests the formation of only localised monoclinic crystals during the plasma treatment process, which may be buried within the noise of the XRD and Raman spectra. Further detailed analysis and identification of these findings in future studies could provide valuable insights into the reduction mechanism of plasma treatment, but it is beyond the scope of

the current study.

Comparable thermal gravimetric (TG) and heat flow curves are obtained for both untreated and plasma treated zirconia during the isothermal holding at 500 °C for 10 h (Fig. 7b). Both sample types exhibit an initial reduction in mass, followed by a gradual increase for the remainder of the testing period. The untreated zirconia undergoes a larger reduction (0.85 % loss at 75 min) and remains below the initial mass for a longer duration (6 h) compared to the plasma treated zirconia (100 min, with a maximum loss of 0.21 % at 45 min).

The heat flow curves for both samples remain relatively flat, indicating steady and continuous oxidation of the zirconia specimens at the higher temperature. However, the heat flow of the plasma treated zirconia is measured to be 520 ± 25 % more exothermic across the final 5 h of the holding stage, with an average heat flow of 0.0304 ± 0.0010 mW.mg^{-1} (as compared with the 0.0049 ± 0.0005 mW.mg^{-1} heat flow of the untreated zirconia). This suggests that significantly more oxidation (or re-oxidation) of the plasma treated zirconia takes place during the holding stage (i.e., $ZrO_{2-x} \rightarrow ZrO_{2-x+d}$, where d is the stoichiometric equivalent addition of oxygen) [53,76].

This hypothesis is further supported by the greater final mass (101.00 ± 0.01 % for plasma treated and 100.44 ± 0.01 % for untreated zirconia) measured across the final 20 min of holding, as well as the more limited initial mass reduction of the plasma treated zirconia. Extrapolating the steady negative heat flow gradient of the plasma treated zirconia over the final 5 h (Fig. 7b; -1.04×10^{-5} mW.mg^{-1}.min^{-1}) suggests that approximately 38.24 additional hours of holding at 500 °C (for a total of 48.24 h) are necessary for the plasma treated zirconia to reach the same heat flow as the untreated zirconia. On the other hand, the untreated zirconia reaches the final stable heat flow value of 0.0049 mW.mg^{-1} after approximately 4 h of isothermal holding at 500 °C. This indicates that the plasma treated zirconia is approximately 12.1 times more oxygen-deficient than the untreated zirconia. On the other hand, the untreated zirconia reaches the final stable heat flow value of 0.0049 mW.mg^{-1} after approximately 4 h of isothermal holding at 500 °C. This indicates that the plasma treated zirconia is approximately 12.1 times more oxygen-deficient than the untreated zirconia.

3.5. Optical absorption capability and electronic band structure

In the case of oxygen-deficient zirconia (ZrO_{2-x}), the introduction of oxygen vacancy defects has shown potential for modifying the intrinsic electronic characteristics, and thus, influencing the electronic band structure, the bandgap (E_g) and the Fermi level (E_f) of the material [12,25,77]. By creating oxygen vacancies with 0 or 1 trapped electrons (i.e., F^{2+} and F^{+} centres, respectively), nearby Zr^{4+} ions can be reduced to Zr^{3+} to maintain charge neutrality (as demonstrated in Eqs. (2) and (3). This reduction of zirconium cations results in the occupation of the 4d energy level in Zr ions, raising the lowest occupied energy level. Due to the various interatomic interactions (e.g., orbital hybridisation, changes in electrostatic potential), this reduction of zirconium cations significantly affects the electronic properties of the bulk material.

Density functional theory (DFT) studies have indicated that this reduction leads to the formation and occupation of new energy states, primarily originating from Zr 4d orbitals, which are approximately 1.2–1.6 eV below the conduction band (CB) of pristine zirconia [11,21,23,25,30,54,62,69,77]. Consequently, this shifts the E_f to a higher energy, reducing the bandgap between the top edge of the valence band (VB) and the bottom edge of the CB. This reduction of the bandgap transforms electrically insulating zirconia into an n-type semiconductor capable of absorbing visible light [72]. Moreover, these newly formed states within the bandgap primarily interact with the conduction band, leading to the trapping of electrons near the CB (trap-assisted recombination). This, in turn, reduces the recombination rates between excited electrons in the CB and holes in the lower energy states of the VB [14,30,78]. Consequently, the electron's lifetime in the conduction band is prolonged, allowing for enhanced absorption of photons across a wider range of energies [23,28,54,59].

Consistent with previous studies on oxygen-deficient zirconia, the plasma treated zirconia in this research exhibit excellent light absorption properties, as observed through both Raman analysis (Fig. 3b) and diffuse reflectance spectroscopy (DRS; Fig. 8) [12,13,25,30,54,59,62,69]. Although Raman analysis was conducted using monochromatic light at 532 nm, the average area of each deconvoluted component of the plasma treated zirconia demonstrated a significant enhancement in light absorption, with an average area reduction of 79.6 ± 3.6 % compared to untreated zirconia. Furthermore, the plasma treated zirconia exhibited an average light absorption of 73.2 ± 5.7 % across the entire DRS range (200–3000 nm), whereas the untreated zirconia only absorbed 44.1 ± 8.5 % of the light. This corresponds to a 66.2 % increase in light absorption capability of the plasma treated zirconia throughout the natural sunlight spectrum.

Moreover, the untreated white zirconia only exhibited notable optical absorption capability in the short-wave ultraviolet (UV) region (Fig. 8), with maximum absorption at approximately 240 nm (equivalent to ≈5.1 eV), consistent with previous studies on the bandgap of zirconia [10,11,62]. In contrast, the black plasma treated zirconia demonstrated excellent (>65 %) absorption across the entire spectrum, including the shortwave infrared (SWIR) range. This represents a significant enhancement in light absorption capability for the plasma treated zirconia, surpassing the performance of oxygen-deficient zirconia reported in other studies, many of which focused on the absorption capabilities of their zirconia materials at wavelengths below 700 nm (UV and visible range). It is worth noting that while UV and visible radiation carry higher energy density compared to near-infrared (NIR) or SWIR radiation, natural sunlight is comprised of only 5 % UV (300–400 nm) and 43 % visible (400–700 nm), with the remaining 52 % consisting of the different categories of infrared (700–2500 nm) radiation. Therefore, the sustained absorption across the entire solar spectrum holds tremendous potential for future efficient solar energy harvesting (i.e., high yield) using plasma generated oxygen-deficient zirconia.

By applying the Tauc method and Kubelka-Munk function (as described in §S3 of the supporting information), the $(F(R)h\nu)^{1/\gamma}$ values were calculated for both untreated and plasma treated zirconia (Fig. 9a& b) [52,79]. This analysis revealed the direct ($\gamma = ½$) and indirect ($\gamma = 2$) bandgaps of the untreated and plasma treated zirconia. Consistent with

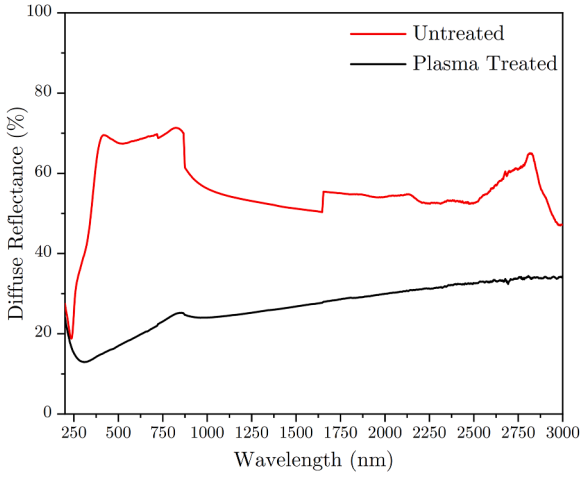

Fig. 8. Diffuse reflectance spectroscopy of untreated and plasma treated zirconia in the wavelength range of 200–3000 nm. The reflectance spectrum of untreated zirconia demonstrates strong reflection (indicating weak absorption) at longer wavelengths, while only exhibiting pronounced absorption at approximately 240 nm (corresponding to a bandgap of ≈5.1 eV). In contrast, plasma treated zirconia exhibits a substantial decrease in reflected light (indicating strong absorption), with less than 35 % reflection observed across the entire spectrum.

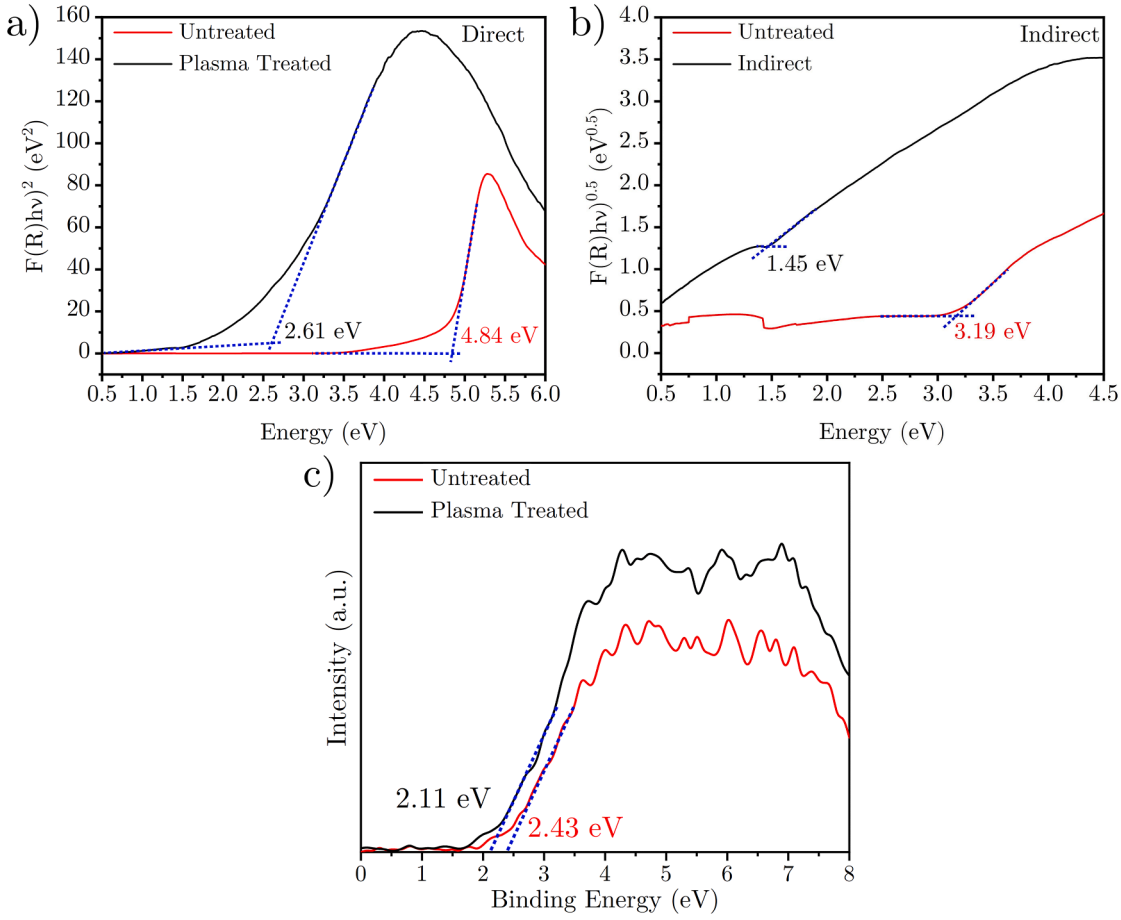

Fig. 9. (a) (a) Direct bandgap (Eg), (b) indirect bandgap, and (c) valence band positions of untreated and plasma treated zirconia. The E_g values are approximated using a combined Tauc method and Kubelka-Munk function, plotted against photon energy. Plasma treated zirconia exhibits significant reductions in both direct bandgap (from 4.84 eV to 2.61 eV) and indirect bandgap (from 3.19 eV to 1.45 eV) compared to untreated zirconia. The absence of a complete plateau or zero absorption value indicates a complex band structure with localised bandgaps that vary considerably. Additionally, the valence band positions of zirconia shift upward towards the conduction band (i.e., lower binding energy) following plasma treatment.

previous literature, the untreated zirconia of this study was extrapolated to have a direct bandgap of 4.84 eV and an indirect bandgap of 3.19 eV [54,80–82]. In contrast, the plasma treated zirconia demonstrated significantly reduced direct and indirect bandgaps, measuring 2.61 eV and 1.45 eV, respectively. These findings align with the expected formation of new bandgaps resulting from the introduction of oxygen vacancies and reduction of zirconium cations. It is important to note that the plasma treated zirconia did not exhibit a complete plateau or zero absorption value under both direct and indirect curves, indicating the presence of a complex band structure (beyond what is depicted in Fig. 10) that could be ascribed to increased trap-assisted recombination events [14,28,59]. As proposed by Qi, et al. [62], the generation of interstitial zirconium (I_{Zr}) defect sites can also contribute to the reduction of the bandgap. Furthermore, Qi, et al. [62] also suggested that I_{Zr} defects primarily enhance longer-wavelength light absorption, such as in the NIR range, while oxygen vacancies promote light absorption across a broad spectrum, with the greatest enhancement in the UV and visible regions [31]. Considering the strong light absorption of the plasma treated zirconia across the wide spectrum (including the SWIR region) and the complex electronic band structure, it is plausible that the plasma treatment of zirconia gives to simultaneous formation of oxygen vacancies and interstitial zirconium migration. However, further investigations are needed to explore this hypothesis in detail.

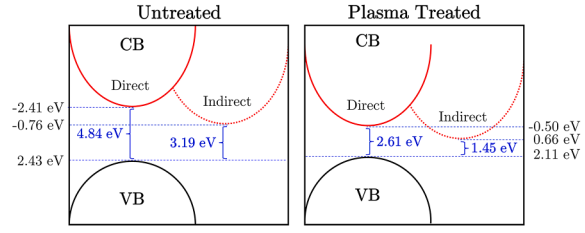

Fig. 10. Calculated energy band diagrams (vs. NHE) of untreated and plasma treated zirconia (using values measured in Fig. 9). Following plasma treatment of the zirconia, the combined downwards movement of the conduction bands (CB) and the slight upwards shift of the valence band (VB) give rise to significantly smaller bandgaps (approximately halved) for both direct (going from 4.84 eV to 2.61 eV) and indirect (going from 3.19 eV to 1.45 eV) transitions.

Low binding energy XPS measurements (Fig. 9c) were conducted to determine the VB positions of untreated and plasma treated zirconia. The results showed that the top edge of the VB for untreated zirconia was at 2.43 eV, while for plasma treated zirconia, it was at 2.11 eV (vs. normal hydrogen electrode (NHE)) [83]. By combining these VB energies with the previously measured direct (Fig. 9a) and indirect (Fig. 9b) bandgap energies, it was possible to estimate the energy of the bottom edges of the CBs and construct energy band diagrams, as shown in Fig. 10. The bottom edges of the CBs for untreated zirconia were measured to be at −2.41 eV (direct) and 0.76 eV (indirect), while for plasma treated zirconia, they were found to be at −0.50 eV (direct) and 0.66 eV (indirect). The observed rise of the VB (−0.32 eV) and the significant tailing of the bottom edge of the CB (1.91 eV for direct and 1.42

eV for indirect bandgaps) in plasma treated zirconia indicate a relative shift of the E_f towards the CB. These findings are consistent with previous studies on oxygen-deficient zirconia, both theoretical and experimental, that suggest the formation of a new donor intra-bandgap level (close to the CB) following the transformation of zirconia due to increasing oxygen-deficiency and reduction of Zr cations [62,78,84].

It has been observed that untreated zirconia lacks intra-bandgap states between the VB and the CB, and the top of the VB is primarily composed of electrons in the oxygen 2p (O 2p) orbital [11,12]. However, plasma treatment of zirconia leads to the creation of vacant oxygen sites, reducing the availability of O 2p orbitals for electron occupation or hole formation. Simultaneously, the reduction of zirconium results in electron occupation of the zirconium 4d orbital, forming an intra-bandgap state close to the bottom of the CB and causing the upward movement of the E_f [62,69]. The reduced bandgap between the Zr 4d energy level and the CB leads to a higher electron density in the CB and an increased density of holes in the Zr 4d energy level (resulting from excitation of Zr 4d electrons into the CB).

Due to the occupation of Zr 4d orbitals and the limited availability of O 2p orbitals, electrons tend to be trapped near the CB and recombine with holes in the VB at a slower rate (due to continuous excitation and relaxation events between the Zr 4d orbital and the CB). This results in a reduced formation of holes in the VB and an increased occupation of electrons in the CB, leading to n-type conductivity in plasma treated zirconia (where electrons predominantly carry electrical current) [23,49,75,78].

3.6. Future perspective of plasma defect-engineering of zirconia

The significant capability and efficiency of plasma treatments for modifying the electronic band structure and optical properties of fully dense zirconia offer promising prospects for scalable, cost-efficient, rapid, and environmentally friendly production of n-type semiconducting zirconia. The adaptability and close control of plasma treatments also open avenues for future optimisation and expansion of this production route. By adjusting various treatment parameters such as temperature, gas mixture, gas pressure, electrode material, electrode power, and treatment configuration, tailored treatments can be developed for different applications, further improving upon the treatment method used in this study [48,85–87]. It is important to note that the choice of hydrogen plasma treatment in this study was selected for its simplicity, with the primary objective of demonstrating the potential of low-pressure plasma treatment to rapidly produce oxygen-deficient zirconia with a low bandgap.

One unique advantage of low-pressure plasma technologies, unlike traditional electrochemical methods, is the ability to physically separate the anode and cathode electrodes, even across large distances [48,88]. This separation is facilitated by the continuous presence of an electrically conductive gas medium during the treatment process. This characteristic opens the prospect to overcome the layer separation phenomenon typically associated with equivalent electrochemical techniques for the formation of oxygen-deficient zirconia. In low-temperature electrochemical methods [43], there is a tendency to form a tri-layer configuration, consisting of (1) n-type conductivity (with high oxygen vacancy and cation reduction) at the cathodic side, (2) p-type conductivity (with high vacancy occupation and low cationic reduction) at the anodic side, and (3) a largely unmodified layer with ionic conductivity at high temperatures sandwiched between the layers (1) and (2).

Considering that, in low-pressure plasma treatments, the electrodes are physically separated, the electrical potential gradient across the anode and cathode is distributed over a larger distance. As a result, there is minimal electrical potential variation in the vicinity of each electrode, which can enable the formation of solely n-type or p-type semiconducting zirconia, depending on the electrode in contact with the material. This has the potential to offer greater flexibility and control when producing semiconducting zirconia materials.

This study serves as a fundamental basis for future advancements in the field of low-pressure plasma treatments, specifically for the development of novel bulk transformed semiconducting zirconia materials. The findings and insights gained from this research can pave the way for the design and optimisation of more complex and industrially viable plasma treatments. The properties and structure of our material suggest that it could be a promising candidate for photocatalysis. However, dedicated experiments are necessary to prove this, which are beyond the scope of this paper and should be considered in future research. By building upon this study, it may also be possible to extend the application of low-pressure plasma treatments to other materials, opening new opportunities for innovative production and development of materials.

4. Conclusions

This study focuses on the novel hydrogen plasma treatment of 3 mol % yttria-stabilised zirconia and investigates its impact on light absorption capability and energy band structure. The research encompasses various analyses, including visual, magnetic, electronic, and thermal assessments, to examine the formation of oxygen vacancies, colour transformation, and structural characteristics of the plasma treated zirconia. The following conclusions can be drawn from this study:

1 After subjecting zirconia to hydrogen plasma treatment at 500 °C for 5 h, a bulk transformation occurs, changing the colour from pristine white to metallic black.
2 Combined DSC and TGA analysis reveal the limited presence of the monoclinic phase in plasma treated zirconia, indicated by a monoclinic-to-tetragonal phase transition between 275 and 400 °C. However, no significant crystallographic or structural changes, such as atomic spacing or bonding environment, are observed across large regions.
3 EPR analysis shows the formation of two new signals corresponding to the presence of Zr3+ cations in plasma treated zirconia. The lack of change in signal at g-tensor value of ≈2.004 suggests that the reduction of zirconium primarily leads to the formation of diamagnetic F2+ ($V_O^{\cdot\cdot}$) centres.
4 XPS analysis demonstrates significantly increased concentrations of oxygen vacancies and reduced zirconium ions (Zr3+) in plasma treated zirconia, as evidenced by changes in O 1 s and Zr 3d spectra.
5 Thermal analysis using DSC and TGA shows continuous exothermic heat flow and mass gain in plasma treated zirconia. Extrapolated estimations indicate that re-oxidation of the zirconia back to its untreated state would require approximately 48 h of holding at 500 °C in air. This corresponds to 12.1 times greater oxygen-deficiency in plasma treated zirconia.
6 Plasma treated zirconia exhibits significantly higher light absorption across the entire sunlight spectrum (200–3000 nm) compared to untreated zirconia. The average measured light absorption for plasma treated zirconia is 73.2 ± 5.7 %, whereas it is 44.1 ± 8.5 % for untreated zirconia. Moreover, plasma treated zirconia demonstrates >65 % light absorption for all wavelengths within the tested spectrum.
7 Plasma treatment leads to a significant reduction in both the direct and indirect bandgap values of zirconia. The direct bandgap decreases from 4.84 eV to 2.61 eV, while the indirect bandgap decreases from 3.19 eV to 1.45 eV. Consistent with previous literature, these changes indicate an upward shift of the valence band edge and a downward shift of the conduction band edge.

Considering the notable benefits offered by low-pressure plasma treatments, such as their ability to accommodate various specimen geometries and minimal electrical potential gradient across the workpiece, we anticipate that our findings will facilitate the cost-effective and efficient production of oxygen-deficient zirconia for advanced energy

materials. In future studies, it would be worthwhile to explore the influence of plasma treatment on the mechanical properties of zirconia, particularly fracture toughness and hardness, which are crucial performance indicators that distinguish zirconia from other ceramic materials. Such investigations will contribute to improving the understanding of the effects of plasma treatment on the overall performance of zirconia materials.

Data availability

Data are available from the corresponding author (F. Shi) or first named author (B. Dashtbozorg) upon reasonable request.

Declaration of generative AI and AI-assisted technologies in the writing process

The contents of the manuscript were manually prepared and edited without the use of generative AI or AI-assisted technologies. OpenAI ChatGPT (GPT-3) was only used to improve readability and language of the manuscript at the final stage. The authors reviewed and edited the content as needed and take full responsibility for the content of the publication.

Declaration of Competing Interest

The authors declare that they have no known competing financial interests or personal relationships that could have appeared to influence the work reported in this paper.

Acknowledgements

One of the authors, F.S, would also like to thank the studentship from the Centre for Doctoral Training in Innovative Metal Processing (IMPaCT) funded by EPSRC, UK (EP/F006926/1). The authors would also like to thank Dr. Hailiang Liao from the Division of Physical Sciences and Engineering at the King Abdullah University of Science and Technology for the XPS measurements of this study.

Supplementary materials

Supplementary material associated with this article can be found, in the online version, at doi:10.1016/j.actamat.2023.119457.

References

[1] Y.T. Huang, S.R. Kavanagh, D.O. Scanlon, A. Walsh, R.L.Z. Hoye, Perovskite-inspired materials for photovoltaics and beyond—from design to devices, Nanotechnology 32 (13) (2021), 132004.
[2] A. Fakharuddin, R. Jose, T.M. Brown, F. Fabregat-Santiago, J. Bisquert, A perspective on the production of dye-sensitized solar modules, Energy Environ. Sci. 7 (12) (2014) 3952–3981.
[3] A. Bartkowiak, O. Korolevych, G.L. Chiarello, M. Makowska-Janusik, M. Zalas, How can the introduction of Zr^{4+} ions into TiO_2 nanomaterial impact the DSSC photoconversion efficiency? A comprehensive theoretical and experimental consideration, Materials 14 (11) (2021) 2955.
[4] X. Chen, S. Shen, L. Guo, S.S. Mao, Semiconductor-based photocatalytic hydrogen generation, Chem. Rev. 110 (11) (2010) 6503–6570.
[5] C.V. Reddy, K.R. Reddy, V.V.N. Harish, J. Shim, M.V. Shankar, N.P. Shetti, T. M. Aminabhavi, Metal-organic frameworks (MOFs)-based efficient heterogeneous photocatalysts: synthesis, properties and its applications in photocatalytic hydrogen generation, CO_2 reduction and photodegradation of organic dyes, Int. J. Hydrog. Energy 45 (13) (2020) 7656–7679.
[6] A. Emeline, G.V. Kataeva, A.S. Litke, A.V. Rudakova, V.K. Ryabchuk, N. Serpone, Spectroscopic and photoluminescence studies of a wide band gap insulating material: Powdered and colloidal ZrO_2 sols, Langmuir 14 (18) (1998) 5011–5022.
[7] V.R. Paiverneker, A.N. Petelin, F.J. Crowne, D.C. Nagle, Color-center-induced band-gap shift in yttria-stabilized zirconia, Phys. Rev. B 40 (12) (1989) 8555–8557.
[8] D.Y.C. Leung, X. Fu, C. Wang, M. Ni, M.K.H. Leung, X. Wang, X. Fu, Hydrogen production over titania-based photocatalysts, ChemSusChem 3 (6) (2010) 681–694.
[9] M. Biesuz, L. Pinter, T. Saunders, M. Reece, J. Binner, V. Sglavo, S. Grasso, Investigation of electrochemical, optical and thermal effects during flash sintering of 8YSZ, Mater 11 (7) (2018) 1214.
[10] D. Manoharan, A. Loganathan, V. Kurapati, V.J. Nesamony, Unique sharp photoluminescence of size-controlled sonochemically synthesized zirconia nanoparticles, Ultrason. Sonochem. 23 (2015) 174–184.
[11] C. Gionco, M.C. Paganini, E. Giamello, R. Burgess, C. Di Valentin, G. Pacchioni, Paramagnetic defects in polycrystalline zirconia: an EPR and DFT study, Chem. Mater. 25 (11) (2013) 2243–2253.
[12] A. Sinhamahapatra, J.P. Jeon, J. Kang, B. Han, J.S. Yu, Oxygen-deficient zirconia (ZrO_{2-x}): a new material for solar light absorption, Sci. Rep. 6 (1) (2016) 27218.
[13] D. Zu, H. Wang, T. Yang, H. Wei, S. Sun, H. Wu, Black ZrO_2 synthesized by molten lithium reduction strategy for photocatalytic hydrogen generation, J. Am. Ceram. Soc. 103 (8) (2020) 4035–4042.
[14] Y. Huang, Y. Yu, Y. Yu, B. Zhang, Solar photocatalysis, Sol. RRL 4 (8) (2020), 2000037.
[15] L. Sun, X. Jiao, W. Liu, Y. Wang, Y. Cao, S.J. Bao, Z. Xu, Y. Kang, P. Xue, Novel oxygen-deficient zirconia (ZrO_{2-x}) for fluorescence/photoacoustic imaging-guided photothermal/photodynamic therapy for cancer, ACS Appl. Mater. Interfaces 11 (44) (2019) 41127–41139.
[16] C. Chen, C. Ruan, Y. Zhan, X. Lin, Q. Zheng, K. Wei, The significant role of oxygen vacancy in Cu/ZrO_2 catalyst for enhancing water–gas-shift performance, Int. J. Hydrog. Energy 39 (1) (2014) 317–324.
[17] C.M. Cristache, M. Burlibasa, G. Cristache, S. Drafta, I.A. Popovici, A.A. Iliescu, S. Zisi, L. Burlibasa, Zirconia and its biomedical applications, Metal. Int. 16 (7) (2011) 18–23.
[18] V. Rani, A. Sharma, A. Kumar, P. Singh, S. Thakur, A. Singh, Q.V. Le, V.H. Nguyen, P. Raizada, ZrO_2-based photocatalysts for wastewater treatment: from novel modification strategies to mechanistic insights, Catalysts 12 (11) (2022) 1418.
[19] Luo Y.R., Kerr J.A., Bond dissociation energies, CRC Handbook of chemistry and physics 89 (2012) 89.
[20] W. Chupka, J. Berkowitz, M.G. Inghram, Thermodynamics of the Zr-ZrO2 system: the dissociation energies of ZrO and ZrO2, J. Chem. Phys. 26 (5) (1957) 1207–1210.
[21] O.A. Syzgantseva, M. Calatayud, C. Minot, Revealing the surface reactivity of zirconia by periodic DFT calculations, J. Phys. Chem. C 116 (11) (2012) 6636–6644.
[22] S. Kouva, K. Honkala, L. Lefferts, J. Kanervo, Review: monoclinic zirconia, its surface sites and their interaction with carbon monoxide, Catal. Sci. Technol. 5 (7) (2015) 3473–3490.
[23] E. Albanese, A. Ruiz Puigdollers, G. Pacchioni, Theory of ferromagnetism in reduced ZrO_{2-x} nanoparticles, ACS Omega 3 (5) (2018) 5301–5307.
[24] A.S. Foster, V. Sulimov, F.L. Gejo, A. Shluger, R.M. Nieminen, Structure and electrical levels of point defects in monoclinic zirconia, Phys. Rev. B 64 (22) (2001), 224108.
[25] Q. Wang, K. Edalati, Y. Koganemaru, S. Nakamura, M. Watanabe, T. Ishihara, Z. Horita, Photocatalytic hydrogen generation on low-bandgap black zirconia (ZrO_2) produced by high-pressure torsion, J. Mater. Chem. A 8 (7) (2020) 3643–3650.
[26] U. Anselmi-Tamburini, J.N. Woolman, Z.A. Munir, Transparent nanometric cubic and tetragonal zirconia obtained by high-pressure pulsed electric current sintering, Adv. Funct. Mater. 17 (16) (2007) 3267–3273.
[27] A. Alvarez, Y. Dong, I.W. Chen, DC electrical degradation of YSZ: voltage-controlled electrical metallization of a fast ion conducting insulator, J. Am. Ceram. Soc. 103 (5) (2020) 3178–3193.
[28] S. Nikiforov, A. Menshenina, S. Konev, The influence of intrinsic and impurity defects on the luminescent properties of zirconia, J. Lumin. 212 (2019) 219–226.
[29] J.S. Moya, R. Moreno, J. Requena, J. Soria, Black color in partially stabilized zirconia, J. Am. Ceram. Soc. 71 (11) (1988) C479–C480.
[30] F. Qi, Z. Yang, J. Zhang, Y. Wang, Q. Qiu, H. Li, Interfacial reaction-induced defect engineering: enhanced visible and near-infrared absorption of wide band gap metal oxides with abundant oxygen vacancies, ACS Appl. Mater. Interfaces 12 (49) (2020) 55417–55425.
[31] H. Lv, J. Bao, F. Ruan, F. Zhou, Q. Wang, W. Zhang, W. Guo, Y. Zhang, X. Song, S. An, Preparation and properties of black Ti-doped zirconia ceramics, J. Mater. Res. Technol. 9 (3) (2020) 6201–6208.
[32] C. Morant, J.M. Sanz, L. Galán, Ar-ion bombardment effects on ZrO_2, Phys. Rev. B 45 (3) (1992) 1391–1398.
[33] J. Janek, C. Korte, Electrochemical blackening of yttria-stabilized zirconia a morphological instability of the moving reaction front, Solid State Ion. 116 (3–4) (1999) 181–195.
[34] J.M. Farley, J.S. Thorp, J.S. Ross, G.A. Saunders, Effect of current-blackening on the elastic constants of yttria-stabilised zirconia, J. Mater. Sci. 7 (4) (1972) 475–476.
[35] D.A. Wright, J.S. Thorp, A. Aypar, H.P. Buckley, Optical absorption in current-blackened yttria-stabilized zirconia, J. Mater. Sci. 8 (6) (1973) 876–882.
[36] J.S. Thorp, H.P. Buckley, The dielectric constants of current-blackened single crystral yttria-stabilized zirconia, J. Mater. Sci. 8 (10) (1973) 1401–1408.
[37] J.S. Thorp, A. Aypar, J.S. Ross, Electron spin resonance in single crystal yttria stabilized zirconia, J. Mater. Sci. 7 (7) (1972) 729–734.
[38] B. Luerßen, J. Janek, S. Günther, M. Kiskinova, R. Imbihl, Microspectroscopy at a moving reduction front in zirconia solid electrolyte, Phys. Chem. Chem. Phys. 4 (12) (2002) 2673–2679.
[39] F.K. Moghadam, T. Yamashita, D.A. Stevenson, Characterization of the current-blackening phenomena in scandia stabilized zirconia using transmission electron microscopy, J. Mater. Sci. 18 (8) (1983) 2255–2259.

[40] K. Ye, K. Li, Y. Lu, Z. Guo, N. Ni, H. Liu, Y. Huang, H. Ji, P. Wang, An overview of advanced methods for the characterization of oxygen vacancies in materials, Trends Anal. Chem. 116 (2019) 102–108.

[41] N.N. Yang, P. Shen, B. Yang, R.F. Guo, Q.C. Jiang, Significant improvement in the wettability of ZrO_2 by molten Al under the application of a direct current, Mater. Des. 111 (2016) 158–163.

[42] Y. Yuan, H. Yu, A. Podpirka, P. Ostdiek, R. Srinivasan, S. Ramanathan, Negative differential resistance in oxygen-ion conductor yttria-stabilized zirconia for extreme environment electronics, ACS Appl. Mater. Interfaces 14 (35) (2022) 40116–40125.

[43] J. Vazquez-Arce, H. Tiznado, R. Kirchheim, Onset of electronic conductivity in nanometer thick films of yttria stabilized zirconia (YSZ) at high electric fields, Acta Mater. 229 (2022), 117826.

[44] Y. Dong, I.W. Chen, Electrical and hydrogen reduction enhances kinetics in doped zirconia and ceria: <scp>II</scp>. Mapping electrode polarization and vacancy condensation in <scp>YSZ</scp>, J. Am. Ceram. Soc. 101 (3) (2018) 1058–1073.

[45] K.Rm Rao, K. Trinadh, C. Nouveau, Glow discharge plasma nitriding of low alloy steel, Mater. Today Proc. 19 (2019) 864–866.

[46] J. Wang, J. Xiong, Q. Peng, H. Fan, Y. Wang, G. Li, B. Shen, Effects of DC plasma nitriding parameters on microstructure and properties of 304L stainless steel, Mater. Charact. 60 (3) (2009) 197–203.

[47] G.J. Li, Q. Peng, C. Li, Y. Wang, J. Gao, S.Y. Chen, J. Wang, B.L. Shen, Effect of DC plasma nitriding temperature on microstructure and dry-sliding wear properties of 316L stainless steel, Surf. Coat. Technol. 202 (12) (2008) 2749–2754.

[48] B. Dashtbozorg, X. Tao, H. Dong, Active-screen plasma surface multi-functionalisation of biopolymers and carbon-based materials–an overview, Surf. Coat. Technol. 442 (2022), 128188.

[49] N. Masó, A.R. West, Electronic conductivity in Yttria-Stabilized zirconia under a small *dc* bias, Chem. Mater. 27 (5) (2015) 1552–1558.

[50] S. Landi, I.R. Segundo, E. Freitas, M. Vasilevskiy, J. Carneiro, C.J. Tavares, Use and misuse of the Kubelka-Munk function to obtain the band gap energy from diffuse reflectance measurements, Solid State Commun. 341 (2022), 114573.

[51] B.D. Viezbicke, S. Patel, B.E. Davis, D.P. Birnie, Evaluation of the Tauc method for optical absorption edge determination: znO thin films as a model system, Phys. Status Solidi B 252 (8) (2015) 1700–1710.

[52] P. Makuła, M. Pacia, W. Macyk, How to correctly determine the band gap energy of modified semiconductor photocatalysts based on UV–Vis spectra, J. Phys. Chem. Lett. 9 (23) (2018) 6814–6817.

[53] J. Shinar, D. Tannhauser, B. Silver, ESR study of color centers in yttria stabilized zirconia, Solid State Commun. 56 (2) (1985) 221–223.

[54] S.R. Teeparthi, E.W. Awin, R. Kumar, Dominating role of crystal structure over defect chemistry in black and white zirconia on visible light photocatalytic activity, Sci. Rep. 8 (1) (2018).

[55] A. Naumenko, N. Berezovska, M. Biliy, O. Shevchenko, Vibrational analysis and Raman spectra of tetragonal zirconia, Phys. Chem. Solid State 9 (1) (2008) 121–125.

[56] Y. Hemberger, N. Wichtner, C. Berthold, K.G. Nickel, Quantification of yttria in stabilized zirconia by Raman spectroscopy, Int. J. Appl. Ceram. 13 (1) (2016) 116–124.

[57] S. Vasanthavel, S. Kannan, Structural investigations on the tetragonal to cubic phase transformations in zirconia induced by progressive yttrium additions, J. Phys. Chem. Solids 112 (2018) 100–105.

[58] J. Chevalier, L. Gremillard, A.V. Virkar, D.R. Clarke, The tetragonal-monoclinic transformation in zirconia: lessons learned and future trends, J. Am. Ceram. Soc. 92 (9) (2009) 1901–1920.

[59] J. Zhang, Y. Gao, X. Jia, J. Wang, Z. Chen, Y. Xu, Oxygen vacancy-rich mesoporous ZrO2 with remarkably enhanced visible-light photocatalytic performance, Sol. Energy Mater. Sol. Cells 182 (2018) 113–120.

[60] R. Ben-Michael, D.S. Tannhauser, J. Genossar, ESR centers in reduced stabilized zirconia, Phys. Rev. B 43 (10) (1991) 7395–7404.

[61] V. Laguta, M. Buryi, P. Arhipov, O. Sidletskiy, O. Laguta, M.G. Brik, M. Nikl, Oxygen-vacancy donor-electron center in Y3Al5O12 garnet crystals: electron paramagnetic resonance and dielectric spectroscopy study, Phys. Rev. B 101 (2) (2020).

[62] F. Qi, Z. Yang, Y. Wang, Q. Qiu, H. Li, Defects in black zirconia responsible for solar energy harvesting, J. Mater. Chem. C 9 (46) (2021) 16732–16740.

[63] S.V. Nikiforov, V.S. Kortov, A.N. Kiryakov, S.F. Konev, A.A. Men'Shenina, Increasing the luminescence yield of zirconia, Tech. Phys. Lett. 43 (12) (2017) 1074–1076.

[64] I. Bobricheva, I. Stavitsky, V. Yermolaev, N. Kotsarenko, V. Shmachkova, D. Kochubey, ESR study of paramagnetic sites in sulfated zirconia, Catal. Lett. 56 (1998) 23–27.

[65] E.V. Frolova, M.I. Ivanovskaya, The origin of defects formation in nanosized zirconia, Mater. Sci. Eng. C 26 (5–7) (2006) 1106–1110.

[66] S. Zhu, X. Zu, L. Wang, R. Ewing, Cesium ion implantation in single crystal yttria-stabilized zirconia (YSZ) and polycrystalline $MgAl_2O_4$-YSZ, Mater. Res. Soc. Online Proc. Libr. 713 (2002).

[67] P. Jakes, E. Erdem, Finite size effects in ZnO nanoparticles: an electron paramagnetic resonance (EPR) analysis, Phys. Status Solidi Rapid Res. Lett. 5 (2) (2011) 56–58.

[68] Q. Lou, J. Zeng, Z. Man, L. Zheng, C. Park, A. Kassiba, Y. Liu, X. Chen, G. Li, The effect of grain boundary on the visible light absorption of $BaTi_{1-x}[Ni_{1/2}Nb_{1/2}]_xO_{3-\delta}$, J. Am. Ceram. Soc. 102 (12) (2019) 7405–7413.

[69] C. Imparato, M. Fantauzzi, C. Passiu, I. Rea, C. Ricca, U. Aschauer, F. Sannino, G. D'Errico, L. De Stefano, A. Rossi, A. Aronne, Unraveling the charge state of oxygen vacancies in ZrO_{2-x} on the basis of synergistic computational and experimental evidence, J. Phys. Chem. C 123 (18) (2019) 11581–11590.

[70] P. Lackner, J. Hulva, E.M. Köck, W. Mayr-Schmölzer, J.I.J. Choi, S. Penner, U. Diebold, F. Mittendorfer, J. Redinger, B. Klötzer, G.S. Parkinson, M. Schmid, Water adsorption at zirconia: from the ZrO_2(111)/Pt_3Zr(0001) model system to powder samples, J. Mater. Chem. A 6 (36) (2018) 17587–17601.

[71] N. Bosio, A. Schaefer, H. Grönbeck, Can oxygen vacancies in ceria surfaces be measured by O1s photoemission spectroscopy? J. Condens. Matter Phys. 34 (17) (2022), 174004.

[72] N.W. Lee, K.R. Yoon, J.Y. Lee, Y. Park, S.J. Pyo, G.Y. Kim, D.H. Ha, W.H. Ryu, Highly conductive off-stoichiometric zirconium oxide nanofibers with controllable crystalline structures and bandgaps and improved electrochemical activities, ACS Appl. Energy Mater. 2 (5) (2019) 3513–3522.

[73] Y. Deligiannakis, A. Mantzanis, A. Zindrou, S. Smykala, M. Solakidou, Control of monomeric Vo's versus Vo clusters in ZrO_{2-x} for solar-light H_2 production from H_2O at high-yield (millimoles.gr^{-1}.h^{-1}), Sci. Rep. 12 (1) (2022).

[74] M. Picquart, T. López, R. Gómez, E. Torres, A. Moreno, J. Garcia, Dehydration and crystallization process in sol-gel zirconia, J. Therm. Anal. Calorim. 76 (3) (2004) 755–761.

[75] A.R. Puigdollers, F. Illas, G. Pacchioni, Structure and properties of zirconia nanoparticles from density functional theory calculations, J. Phys. Chem. C 120 (8) (2016) 4392–4402.

[76] J. Malek, S. Matsuda, A. Watanabe, T. Ikegami, T. Mitsuhashi, Crystallization kinetics of zirconia-yttria gels, Thermochim. Acta 267 (1995) 181–194.

[77] M. Lindgren, I. Panas, Oxygen vacancy formation, mobility, and hydrogen pick-up during oxidation of zirconium by water, Oxid. Met. 87 (3–4) (2017) 355–365.

[78] S. Heiroth, R. Ghisleni, T. Lippert, J. Michler, A. Wokaun, Optical and mechanical properties of amorphous and crystalline yttria-stabilized zirconia thin films prepared by pulsed laser deposition, Acta Mater. 59 (6) (2011) 2330–2340.

[79] P.R. Jubu, O. Obaseki, A. Nathan-Abutu, F. Yam, Y. Yusof, M. Ochang, Dispensability of the conventional Tauc's plot for accurate bandgap determination from UV–vis optical diffuse reflectance data, Res. Opt. 9 (2022), 100273.

[80] L.K. Dash, N. Vast, P. Baranek, M.C. Cheynet, L. Reining, Electronic structure and electron energy-loss spectroscopy of ZrO_2 zirconia, Phys. Rev. B 70 (24) (2004).

[81] S.M. Chang, R.A. Doong, Interband transitions in sol−gel-derived ZrO_2 films under different calcination conditions, Chem. Mater. 19 (19) (2007) 4804–4810.

[82] V. Milman, A. Perlov, K. Refson, S.J. Clark, J. Gavartin, B. Winkler, Structural, electronic and vibrational properties of tetragonal zirconia under pressure: a density functional theory study, J. Condens. Matter Phys. 21 (48) (2009), 485404.

[83] T. Götsch, A. Menzel, E. Bertel, M. Stöger-Pollach, S. Penner, The crystallographic and electronic phase diagrams of yttria-stabilized zirconia model electrolytes, ECS Trans. 78 (1) (2017) 311–319.

[84] D.R. Islamov, V.A. Gritsenko, T.V. Perevalov, V.S. Aliev, V.A. Nadolinny, A. Chin, Oxygen vacancies in zirconium oxide as the blue luminescence centres and traps responsible for charge transport: part II—films, Materialia 15 (2021), 100980.

[85] T. Czerwiec, H. Michel, E. Bergmann, Low-pressure, high-density plasma nitriding: mechanisms, technology and results, Surf. Coat. Technol. 108 (1998) 182–190.

[86] M. Łępicka, M. Grądzka-Dahlke, Direct current and pulsed direct current plasma nitriding of ferrous materials a critical review, Acta Mech. Autom. 10 (2) (2016) 150–158.

[87] X. Tao, T.J. Collins, Q. Ao, H. Liu, B. Dashtbozorg, X. Li, H. Dong, Active screen plasma nitriding of Fe-24Mn-2Al-0.45 C TWIP steel: microstructure evolution and a synergistic selective oxidation mechanism, Acta Mater. 241 (2022), 118418.

[88] K. Lin, X. Li, Y. Sun, X. Luo, H. Dong, Active screen plasma nitriding of 316 stainless steel for the application of bipolar plates in proton exchange membrane fuel cells, Int. J. Hydrog. Energy 39 (36) (2014) 21470–21479.